Charge-Mediated Copper-Iodide-Based Artificial Synaptic Device with Ultrahigh Neuromorphic Efficacy

Dani S. Assi, Hongli Huang, Kadir Ufuk Kandira, Nasser S. Alsulaiman, Vaskuri C. S. Theja, Hasan Abbas, Vaithinathan Karthikeyan,* and Vellaisamy A. L. Roy*

In the realm of artificial intelligence, ultrahigh-performance neuromorphic computing plays a significant role in executing multiple complex operations in parallel while adhering to a more biologically plausible model. Despite their importance, developing an artificial synaptic device to match the human brain's efficiency is an extremely complex task involving high energy consumption and poor parallel processing latency. Herein, a simple molecule, copper-iodide-based artificial synaptic device demonstrating core synaptic functions of human neural networks is introduced. Exceptionally high carrier mobility and dielectric constant in the developed device lead to superior efficacies in neuromorphic characteristics with ultrahigh paired-pusle facilitation index (>195). The results demonstrate biomimetic capabilities that exert a direct influence on neural networks across multiple timescales, ranging from short- to long-term memory. This flexible reconfiguration of neural excitability provided by the copper-iodide-based synaptic device positions it as a promising candidate for creating advanced artificial intelligence systems.

D. S. Assi, H. Huang, K. U. Kandira, N. S. Alsulaiman, V. C. S. Theja, H. Abbas, V. Karthikeyan
Electronics and Nanoscale Engineering
James Watt School of Engineering
University of Glasgow
Glasgow G12 8QQ, UK
E-mail: vaithinathan.karthikeyan@glasgow.ac.uk

V. C. S. Theja
Department of Materials Science and Engineering
City University of Hong Kong
Kowloon Tong, Hong Kong

V. A. L. Roy
School of Science and Technology
Hong Kong Metropolitan University
Ho Man Tin, Hong Kong
E-mail: vroy@hkmu.edu.hk

The ORCID identification number(s) for the author(s) of this article can be found under https://doi.org/10.1002/pssr.202300191.

1. Introduction

Artificial intelligence (AI) technologies have radically transformed modern lifestyles over the last few decades using the quantum computing and machine learning (ML) and internet of things (IoT).[1–3] Despite this progress, the standard for these new technologies continues to rely on the traditional von Neumann computer architecture, which presents significant challenges in processing speed and computational power.[4,5] Therefore, achieving this fundamental goal in computing is possible only through the development of effective neuromorphic systems, with specific design to imitate the structure and functionality of the human brain.[6,7] In biological neural networks, neurons and synapses are two fundamental units. The human brain is a highly complex 3D interconnection network space composed of $\approx 10^{11}$ neurons connected through $\approx 10^{15}$ synapses, which underlines all human behaviors, thoughts, and perceptions.[8,9] Despite this remarkable complexity, the human brain consumes only around 20 W of power, unlike supercomputers, which consume $\approx 10^7$ times more than a biological neural network (NN). Moreover, it is estimated that computing devices consume over 8% of global electricity, a rate that is doubling every decade.[10,11] This underscores the pressing need to develop new functional materials and architectural designs for implementing neuromorphic computation systems.

Previously, artificial synapses that can biomimic fundamental human neural network functions are based on Si–cMOS architecture. However, these conventional devices are significantly challenged by their crucial performance metrics such as scalability and energy consumption to improve their neuromorphic sensory efficacies even further.[12] In this aspect, two-terminal memristor devices provide more advantages in emulating synaptic functions where the device resistance level can be continuously tuned by modulating the applied voltage and current, leading to a significant reduction in energy consumption and complexity.[13] The point-to-point architecture of the memristor, where two electrodes are layered between active film, is a perfect structural substitute for the biological synapse, where two neighboring neurons are connected through synapses.[14] Thus, the modulation of the synaptic weight and transmission characteristics of the biological synapse is well

mimicked by the tuneable resistance property of the memristor.[15] To fully complete the biomimicking process, the functional material of the artificial synapse must provide an extensive response to a magnetic, electric, chemical, and optical stimulus while maintaining ultralow power consumption compared to our brain.[16]

In this work, we develop an artificial synaptic device combining the point-to-point memristor array structure with the unique conduction properties in copper iodide (CuI).[17,18] This functional properties in the CuI structure provides promising possibilities to enhance performance in memorization and complex learning operations in a more biologically plausible manner. We have fabricated a neuromorphic synaptic device using a combination of optimized vacancy defects proportions in CuI matrix.[19] Our results indicate superior neuromorphic behaviors based on a precise analysis of synaptic mechanisms and behavior involving trapping and detrapping characteristics. Our insights demonstrate the potential of using a CuI-based artificial synaptic device as a compelling synapse model for forthcoming neuromorphic computing systems.

2. Results and Discussion

2.1. CuI Thin Film Development and Characteristics

Figure 1a illustrates the systematic development of CuI-based synaptic device array via physical vapor deposition process. Here in the synaptic array design, the active functional CuI is deposited in between aluminum electrodes representing the artificial synaptic model with pre- and postsynaptic neurons. Figure 1b shows the field emission scanning electron microscopy (FESEM) image of thin film CuI deposited by thermal evaporation process, demonstrating a uniform formation of microcrystalline layer. To analyze the surface roughness of the microcrystalline thin film, we have performed atomic force microscopy study as shown in Figure 1c, which indicates the deposition of nanocrystalline morphology and the thin film texture shows a surface roughness value of 7.5 nm. Surface texture and roughness are important parameters for optimizing the charge transport in the active material, as the compact thin film
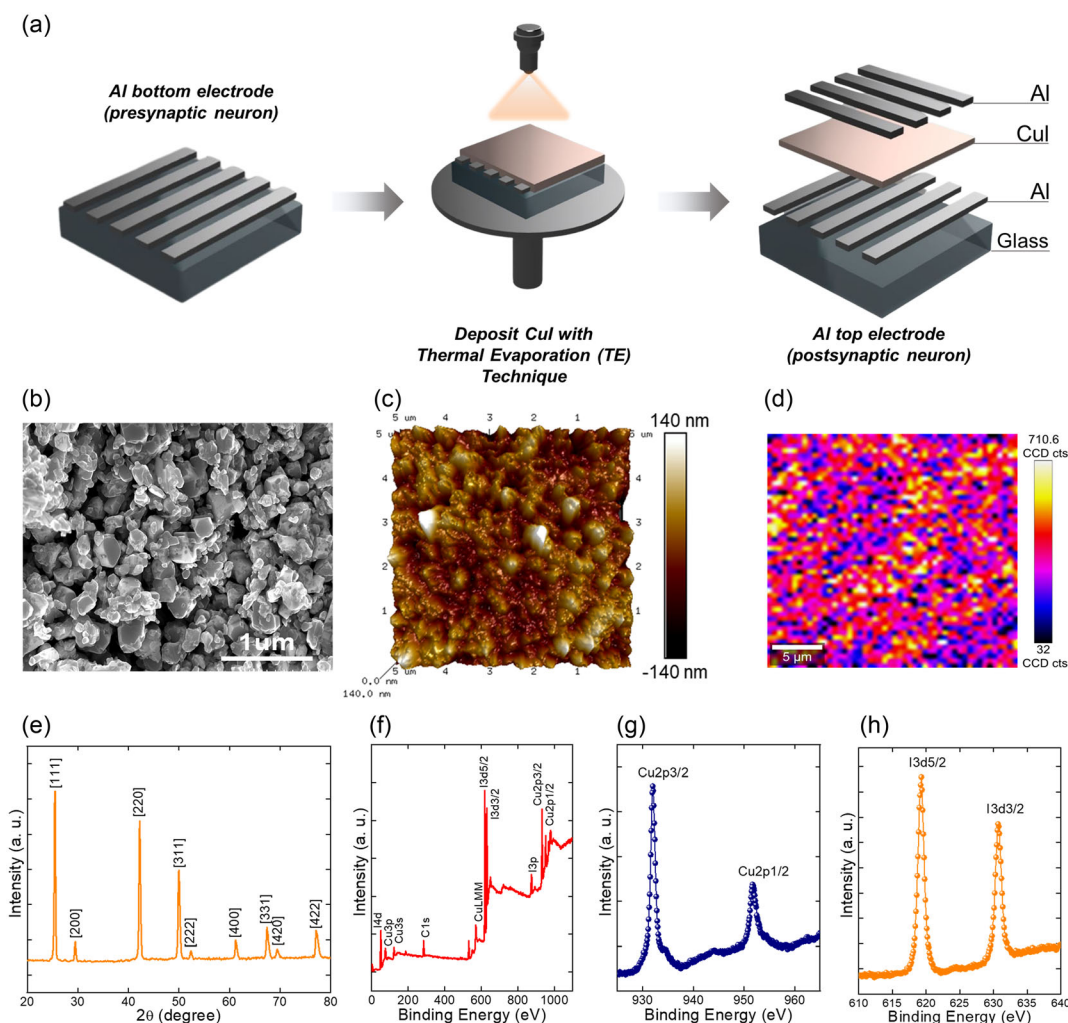

Figure 1. Material characterization of CuI: a) fabrication process steps in CuI-based artificial synaptic device; b) FESEM morphology illustration of the CuI thin film; c) AFM representation of the CuI thin film; d) Raman mapping illustration of the CuI thin film; e) XRD analysis demonstrating characteristic peaks of CuI thin film; f) XPS full scan survey representing the CuI with C 1s as reference; g) high-resolution XPS for Cu 2p peaks; h) high-resolution XPS for I 3d peaks.

surface influences the moderation of carrier scattering. Further to investigate the material composition, we have performed the Raman and X-ray powder diffraction (XRD) studies as shown in Figure 1d,e, respectively. Raman spectroscopy results show the presence of the signature transverse mode peaks of CuI at 91 and 124 cm^{-1}; the mapping demonstrates their uniform distribution of γ phase. The indexed XRD peaks of deposited thin films confirmed the formed γ phase CuI (JCPDS card no.: 06-0246) substrate without any secondary impurity peaks. γ-CuI is a p-type wide bandgap semiconductor with a pure nonlayered cubic crystal structure (zinc-blende type structure with lattice parameters $a = b = c = 6.034$ Å) with a space group of $F\bar{4}3m$. The X-ray photoelectron spectroscopy (XPS) full survey scan is shown in Figure 1f–h where carbon C 1s peaks at 284.6 eV are used as reference peaks. The full scan survey peaks in Figure 1f demonstrates the high purity CuI without any secondary or oxide elemental peaks.

High-resolution XPS spectrum for copper shows two prominent peaks of Cu 2p that corresponds to the Cu 2p$_{1/2}$ and Cu 2p$_{3/2}$ states at 932.3 and 952.0 eV, respectively. High-resolution scan for Iodine spectra of I$^-$ shows prominent peaks corresponding to I 3d$_{3/2}$ and I 3d$_{5/2}$ at 630.8 and 619 eV, respectively. Thus, from the XPS spectra of Cu 2p and I 3d, it implies the successful production of high-purity CuI via thermal deposition.

2.2. Synaptic Switching Mechanism

In the human neural system, the biological synapse serves as a connection bridge between two adjacent neurons.[20] Synergistically, our designed artificial synaptic device architecture effectively emulates the structural and functional behaviors of the biological neural network. To gain a deeper understanding of the electrical properties and switching mechanisms inherent in the CuI-based synaptic device, an analysis of the I–V characteristics of the device is conducted. The device demonstrates repeatable bistable-resistive switching characteristics at room temperature. **Figure 2**a illustrates the nonvolatile memory characteristics with an ultralow threshold voltage (V_{SET}) of 0.2 V and a large on/off ratio of 10^5. The acquired I–V results have been subjected to linear analysis to investigate the conduction mechanism of the developed synaptic device. As illustrated in Figure 2b, the transition process from a high-resistance (HRS) to a low-resistance state (LRS) is characterized by a unique conduction mechanism represented by four distinct regions labeled from A to D. Figure 2c illustrates the thermionic emission limited conduction (TELC) model described by Equation (1), where q, k, I, ε, V, T, E_e, and ϕ represents the respectively electronic charge, Boltzmann's constant, current, relative permittivity, applied voltage, absolute temperature, the activation energy of electrons, and barrier height, respectively.[21] This model elucidates the injection of electrons into the active layer of the device by overcoming the energy barrier through thermal activation.

$$I \propto A \times T^2 \exp\left[-\frac{q\phi_0}{kT} + q\left(\frac{q^3 V}{4\pi\varepsilon}\right)^{\frac{1}{2}}\right] \tag{1}$$

The subsequent region shown in Figure 2d exhibits a linear relationship between voltage and current, known as the Ohmic conduction model, which is described by Equation (2).[21]

$$I \propto V \exp\frac{(-\Delta E_e)}{kT} \tag{2}$$

Figure 2e,f demonstrates space-charged-limited-current (SCLC) model that follows the Child's law based on Equation (3) and trapped-charged-limited-current (TCLC) model, respectively.[21]

$$I \propto V^\alpha \tag{3}$$

The results obtained from regions C and D confirm that the primary mechanism of our device is based on trapping and detrapping charges at the interfaces between the grains within the thin film, which can be enhanced by the migration of Cu^{2+} defects. As the voltage applied to the presynaptic neuron increases, the charge mobility gradually increases, leading to a progressive filling of the defect traps. Upon surpassing the voltage threshold, the transition from the HRS to LRS is accomplished, indicating that nearly all the defect traps are occupied. Conversely, when a reverse voltage bias is applied, the process of detrapping is initiated. Electrical charges function in artificial synaptic devices is analogous to the behavior of neurotransmitters in the human brain; both serve to transmit signals from the pre- to postsynaptic neuron as electrical and chemical messengers, respectively[22] The representation of the nonbiased, SET and RESET states of the artificial synaptic devices are shown in Figure 2g–i.

Overcoming the drawbacks of the huge energy consumption in silicon-based neuromorphic computing devices,[2,14] our developed artificial synaptic device based on the CuI active layer exhibits ultralow-powered synaptic switching characteristics. Energy consumption for the synaptic operations are calculated from the relation Equation (4)

$$E = \int V(t) I(t) dt \tag{4}$$

where voltage V is the applied synaptic switching potentials, I is the corresponding synaptic current, and t is the synaptic switching time.[22] Our device demonstrates low energy consumption ≈ 200 pJ during the synaptic switching.

2.3. Neuromorphic Sensory System

The mammalian brain's capacity for synaptic plasticity allows for the dynamic modulation and adaptation of neural circuit activity, thereby regulating critical synaptic operations that underlie cognitive processes such as learning and memory. These properties are governed by the principle of Hebbian Synaptic Plasticity (HSP) and are characterized with the strengthening/weakening of the connection between two neighboring neurons, known as synaptic weight.[23–25] The modulation of the synaptic strength is governed by two classic Hebbian mechanisms in the human neural system, spike-time (STDP) and spiking-rate-dependent plasticity (SRDP). Here, the SRDP depends on the action potential firing rate and plays a direct role in brain cognitive functions and behavior.[26,27] To characterize and validate neural behaviors in
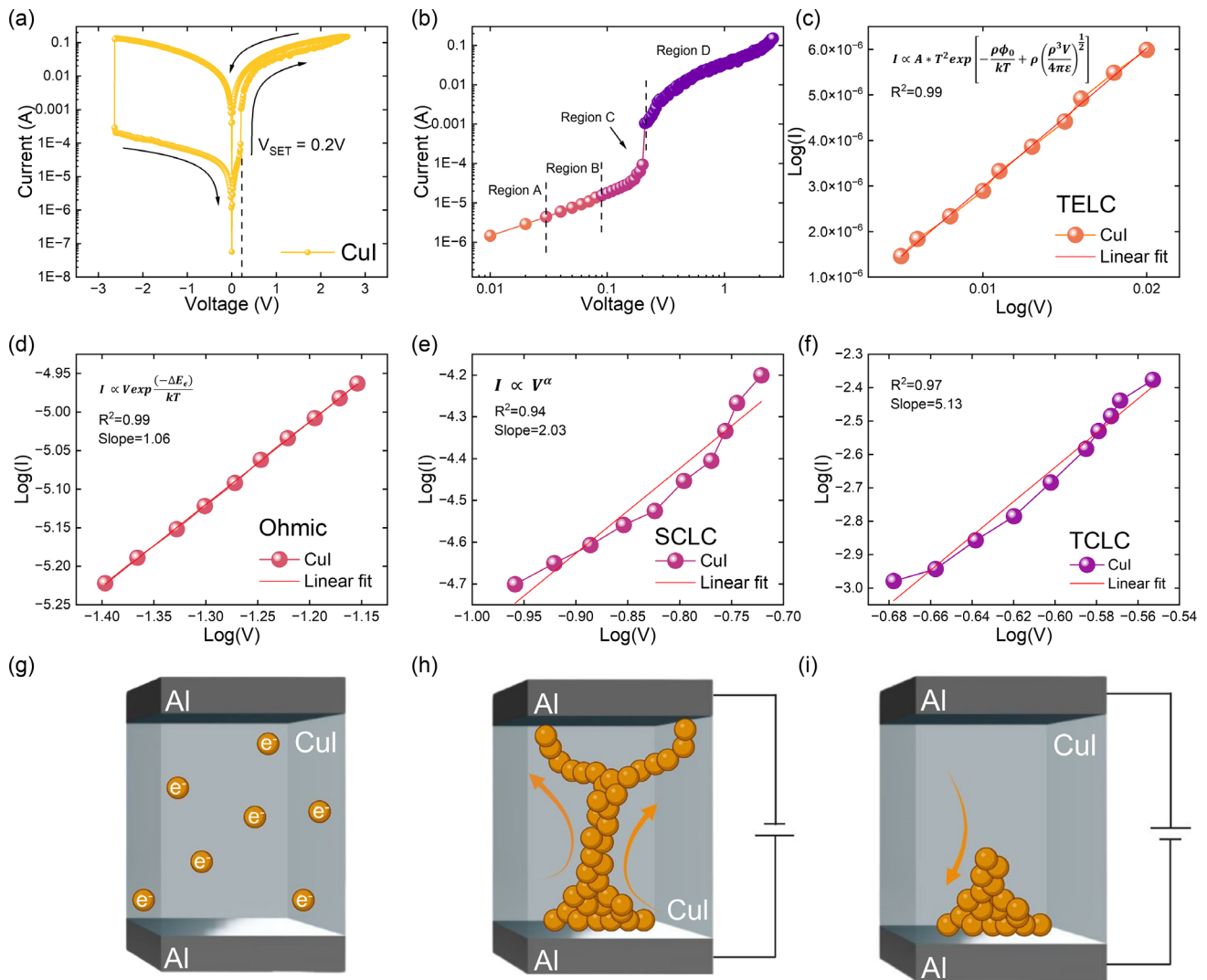
Figure 2. Switching characterization of the artificial synaptic device: a) IV switching characteristics of CuI-based synaptic device; b) the transition process from a high- to low-resistance state is characterized by four distinct conduction mechanism regions involved in the process; c) region A represents thermionic emission limited conduction (TELC) model; d) region B shows Ohmic conduction mode; e) region C demonstrate SCLC model; f) region D represents TCLC model; g) schematic diagram of working flow for under nonbiased conditions; h) under threshold SET voltage; and i) under threshold RESET voltage condition.

our artificial synaptic device, we deeply investigate alterations in excitatory postsynaptic current response following Hebbian-based SRDP method. **Figure 3**a illustrates the emulation pathway of the artificial synaptic device from the human neural system. Figure 3b illustrates the excitatory postsynaptic current (EPSC) response to ten consecutive presynaptic stimuli, with a fixed pulse width of 10 ms and varying pulse intervals between 10 ms to 1 s. It is observed that the synaptic response increases as the pulse interval decreases due to the accumulation of charges in the active CuI layer (trapping/detrapping mechanism). The synaptic efficacy as a function of pulse interval time is demonstrated in Figure 3c, which indicates the successful replication of the biological synaptic responses in our neuromorphic device, thereby establishing the direct correlation between the synaptic weight and presynaptic spiking rate.

In the human nervous system, the ability of postsynaptic neurons is to enhance the synaptic weight for decoding real-time information that are closely linked to paired-pulse facilitation, which represents the form of short-term plasticity. This phenomenon occurs when a pair of shortly spaced stimuli are repeatedly applied to a synapse, leading to an increase in the response strength of the second stimulus.[28–32] The facilitation ratio, which is an index of paired-pulse facilitation, provides a quantitative measure of short-term synaptic efficiency, as expressed by Equation (5), where A_1 and A_2 factors represent the first and second applied stimuli.

$$\text{PPF index} = 100\% \times \frac{A_2}{A_1} \tag{5}$$

The results indicate a direct correlation between the amplitude of the excitatory postsynaptic current and the duration of the
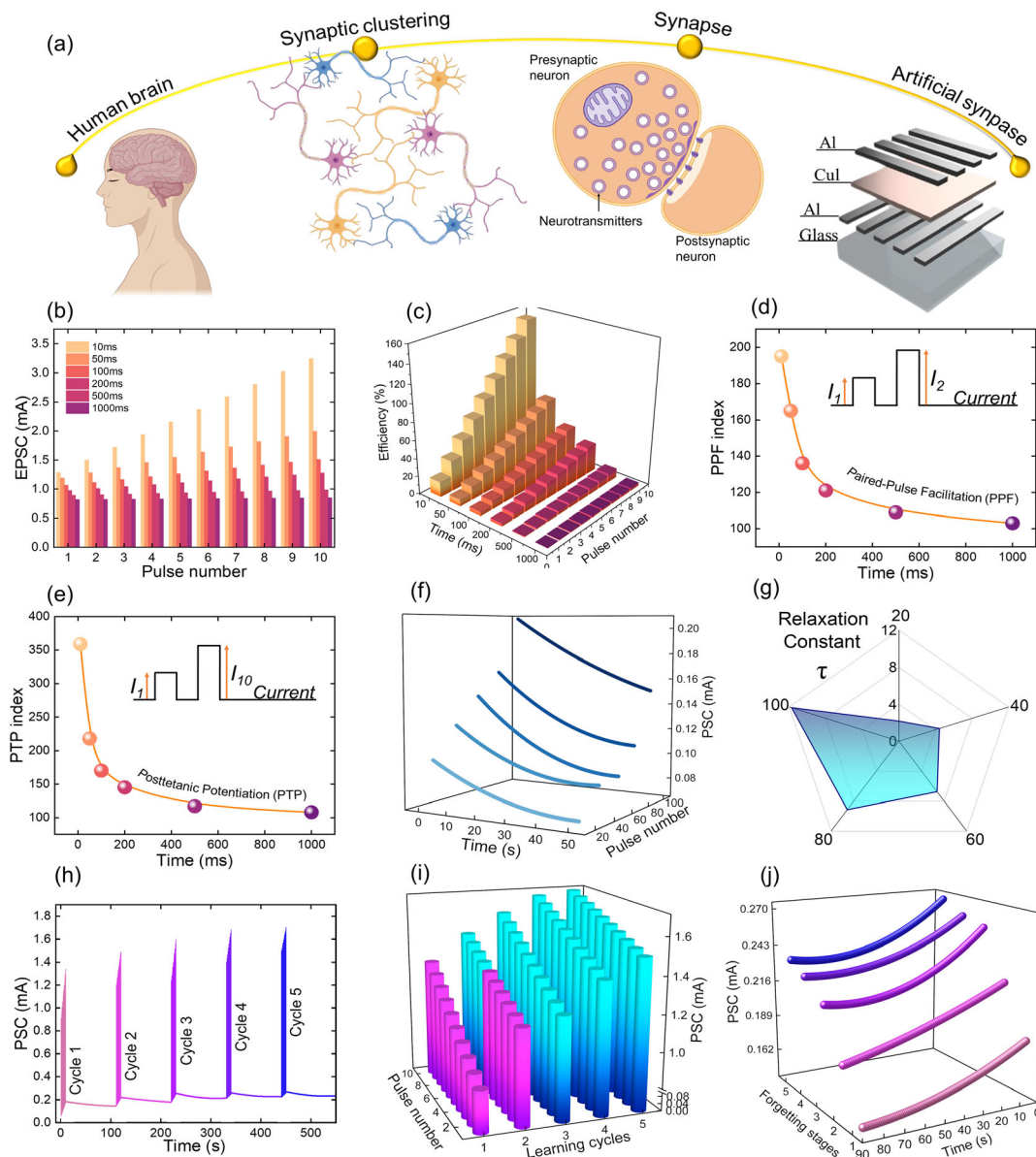
Figure 3. Artificial synaptic devices behaviors: a) emulation pathways from the human neural system to neuromorphic device; b) EPSC responses of our artificial synaptic device when subjected to 10 train stimuli with varying interval time ranging from 10 ms to 1 s; c) efficiency of the synaptic plasticity change based on different pulse intervals (from 10 ms to 1 s); d) PPF index; and e) PTP index is expressed as a function of the paired stimuli applied to the presynaptic neuron with varying time intervals, f) postsynaptic current response to the transition process from short-term plasticity (STP) to long-term plasticity (LTP) in our synaptic device; g) calculated relaxation constant for each pulse cycle during the transition process from STP to LTP; h) the post-synaptic current response was evaluated by emulating the learning–forgetting–relearning function within our synaptic device; i) representation of 5 cycles corresponding learning and relearning behaviors (during the learning cycle—first cycle, the use of purple indicates the established level of postsynaptic current response, while the use of blue indicates that the PSC level is exceeded during the memorization event; j) artificial synaptic device demonstrates the relationship between forgetting behavior and the postsynaptic current response, as observed after every cycle of learning/relearning.

pulse interval, suggesting that a shorter interval between stimulations leads to higher paired-pulse facilitation (PPF) efficiency, as shown in Figure 3d. To further investigate the time-dependent modulation of an artificial synaptic device, we have implemented an emulation of post-tetanic potentiation (PTP), a longer-lasting form of neural facilitation, to evaluate the efficacy of synaptic strengthening.[33] The quantification of this function is expressed through the PTP index, which represents the ratio between the

response to the last pulse stimulus (A_{10}) and the initial one (A_1), as defined by Equation (6).

$$\text{PTP index} = 100\% \times \frac{A_{10}}{A_1} \tag{6}$$

Figure 3e illustrates the efficacy of the PTP index based on pulse interval, closely resembling the long-lasting synaptic effects of PPF behavior observed in the biological neural system.

Table 1. Comparison of the PPF synaptic function (PPF index) by different active material in synaptic devices.

Nos.	Active material	Three/two terminals	Synaptic function	Maximum PPF index [%]	Δt [ms]	Reference
1	ZnO/PbS	Two	SRDP, PPF, PTP STP, LTP	143	≈ 200	[45]
2	$PEA_2MA_{n-1}Pb_nI_{3n+1}$	Two	PPF, STP, LTP	135	10	[46]
3	MoS_2/p-Si	Two	PPF, STP, LTP, STD, LTD	120	1000	[47]
4	Pentacene/PMMA/C_3N_4	Three	PPF, STP, LTP	120	40	[48]
5	$AgBiI_4$	Two	PPF, LTP	30	≈ 0.05	[49]
6	Bi_2O_2Se/graphene	Three	SRDP, PPF, STP, LTP, LTD, L-F-R	120	≈ 100	[50]
7	PAN/C8-BTBT	Three	PPF, STP, LTP, L–F–R	176	≈ 100	[51]
8	$CH_3NH_3PbBr_3$	Two	PPF, STP, LTP	91	80	[52]
9	PVN/PDVT	Three	PPF, PPD STP, LTP	49	≈ 10	[53]
10	HfS_2	Three	PPF, STP, LTP, LTD	111	1000	[54]
11	CuI	Two	SRDP, PPF, PTP, STP, LTP, L–F–R	195	10	This work

Additionally, to conduct a thorough examination of the synaptic behaviors associated with memory retention within biological neural systems, we have employed the human brain model proposed by Atkinson and Schefflin in 1968.[34] This model provides a fundamental understanding of the processes of learning and forgetting, which are consolidated through repeated rehearsal learning. Memorization events within biological neural systems depend on two distinct types of synaptic plasticity, specifically short-term plasticity (STP) and long-term plasticity (LTP), which are determined by the length of memory retention. STP plays a crucial role in synaptic computation, encompassing the processing and decoding of incoming information. At the same time, LTP is responsible for monitoring neural plasticity in the context of memory and learning.[35–38] To assess the viability of our synaptic device's ability to transition from STP to LTP, we have administered a series of consecutive train stimuli consisting of 20, 40, 60, 80, and 100 pulses to the presynaptic membrane while maintaining pulse interval of 100 ms and a pulse amplitude of 100 mV. Figure 3f illustrates the successful transition process between STP and LTP in our artificial synaptic device. The acquired results have been fitted and analyzed with an exponential equation commonly utilized as a forgetting function (Equation (7)) in psychology to extract the relaxation time

$$I = I_0 + A\exp\left(-\frac{t}{\tau}\right) \tag{7}$$

where A represents a constant, I_0 denotes a current constant, and τ measures the relaxation constant, reflecting the rate of decay. Based on the data presented in Figure 3g, it can be observed that the relaxation time demonstrates an increasing trend as the applied pulse stimuli increase from 20 to 100.

The dynamic adaptability of the mammalian brain, driven by its memory formation, storage, and retrieval capabilities, enables it to constantly acquire new experiences and information. The capacity to replicate the learning–relearning–forgetting behavior allows for a more biologically plausible approach to emulating the human neural system.[39–43] Figure 3h demonstrates the administration of 100 training stimuli to the presynaptic neuron, distributed across 5 cycles, with each cycle consisting of 20 pulses. The initial cycle is commonly referred to as the memorization stage, while subsequent cycles are considered relearning stages. After each cycle, spontaneous relaxation decay occurs, which is commonly known as the forgetting stage. Figure 3i illustrates the effectiveness of the developed artificial synaptic device in enhancing memorization capabilities. The results obtained confirm the high efficiency of the synaptic device, as it only requires a single relearning cycle to exceed the established synaptic weight level achieved during the learning operation. The enhancement in efficiency can be attributed to the trapped-charged limited current mechanism inherent in our artificial synaptic device. The process of relearning enables a more capable recollection of previously forgotten memories, resulting in significant time and energy savings compared to the acquisition of new learning. From Figure 3j, we note that forgetting stages as a function of postsynaptic current response increase with each cycle, implying an enhancement of synaptic strength as the number of learning repetition accumulates. **Table 1** provides a comparative analysis of the PPF indexes across various reported synaptic devices, where CuI-based synaptic device exhibits a superior neuromorphic characteristic among them.

3. Conclusion

We have successfully fabricated and demonstrated a charged-based artificial synaptic device that effectively mimics the wide range of synaptic functions in a biologically plausible manner. The optimized composition of the CuI thin layer demonstrates remarkable repeatable synaptic switching characteristics with energy efficient properties. Our results demonstrate that the developed artificial synaptic device is capable of neuromodulating synapses by precisely tuning their plasticity behavior in response to time-dependent factors. Furthermore, the results of synaptic weight and the connection strength modulation between adjacent neurons to initiate transition from short-term and long-term synaptic plasticity are demonstrated. Neuromorphic learning–forgetting–relearning characteristics show higher efficacies which supports enabling the real-time integration of new experiences and information continuously. Thus, our results on CuI-based artificial synaptic devices realize the development of next-generation neuromorphic brain–computer interfaces with unparalleled excitability neural characteristics.

4. Experimental Section

Device Fabrication: CuI thin film was synthesized through the solution process, utilizing iodine pellets (99.99%) and copper powder (99.99%). A 1M iodine solution was meticulously prepared in ethanol, into which copper metal powder was introduced which is subsequently stirred for 5 h at 80 °C. The resultant product is washed and collected after thoroughly rinsed with ethanol and dried in vacuum. The synthesized CuI powder was used for the thin film formation via thermal evaporation technique with thickness of 100 and a 50 nm aluminum film as top and bottom electrodes.

Material Characterization: Structural characteristics of CuI thin film were verified for each sample using the powder XRD Bruker D2 diffractometer with Cu Kα ($\lambda = 1.54$ Å) radiation in the 2θ of 20–80° with a step size of 0.02°. Raman properties were confirmed by Renishaw InVia confocal Raman spectroscopy with a 532 nm laser. FE-SEM FEI Nova NanoSem 630 was used to understand the surface morphology. AFM Bruker Dimension HPI was used to understand surface roughness. The scan size was set up for 2 nm with a scan rate of 0.996 Hz. The X-ray photoelectron spectrometer (Model: Thermo Fisher ESCALAB XI + XPS) was performed to investigate the phase interactions and their bondings.

Electrical Characterization: The resistive switching characteristics of the Al/CuI/Al device were analyzed using the Agilent Technologies B1500A Semiconductor Device Analyzer. The neuromorphic characteristics were evaluated by analyzing the time domain in which various pulse intervals were applied to the presynaptic neuron of the artificial synapse. The obtained results were recorded using a digital storage oscilloscope.

SRDP: To assess the characteristics of SRDP, the artificial synaptic device was subjected to ten consecutive presynaptic pulse stimuli with a fixed pulse width of 100 ms and a pulse amplitude of +100 mV, at intervals of 10, 50, 100, 200, 500, and 1000 ms. The resulting EPSC response was measured and analyzed.

PPF: The process of identifying the PPF function involved the deployment of two sequential train stimuli to the presynaptic neuron, encompassing a diverse range of pulse intervals extending from 10 ms to 1 s. Throughout the measurement process, the pulse width and pulse amplitude remained fixed at 100 ms and +100 mV millivolts, respectively. The PPF index was determined utilizing the formula PPF index $= A_2/A_1$. In this equation, A_1 and A_2 symbolize the postsynaptic current responses evoked by the initial and subsequent pulses, respectively.

PTP: To determine the PTP function, a series of ten successive train stimuli were administered to the presynaptic neuron, with pulse intervals diverging between 10 ms and 1 s. Throughout the measurement process, the pulse width and pulse amplitude remained fixed at 100 ms and +100 mV millivolts respectively. The PTP index was determined utilizing the formula PPF index $= A_{10}/A_1$, where A_1 and A_{10} represent the postsynaptic current (PSC) responses of the first and tenth pulses, respectively.

Transition Process from Short-Term Potentiation (STP) to Long-Term Potentiation (LTP): In order to assess the potential of our synaptic device to transition from STP to LTP, we implemented a series of continuous train stimuli. These stimuli comprised sequences of 20, 40, 60, 80, and 100 pulses, which were administered to the presynaptic neuron. Throughout this procedure, a pulse interval of 100 ms and a pulse amplitude of +100 mV were maintained. The obtained results were processed and evaluated using an exponential equation frequently utilized as a forgetting function within the field of psychology ($I = I_0 + A \times e^{(-t/\tau)}$). In this equation, I_0 represents a constant current, A represents a constant amplitude, and τ measures the relaxation constant, reflecting the rate of decay, which is the value of interest.

Learning–Forgetting–Relearning Process (L–F–R): The processes of memorization and forgetting were determined by the application of 100 training stimuli to the presynaptic neuron, dispersed over five distinct cycles, each encompassing 20 pulses. Throughout the measurement process, the pulse width and pulse amplitude remained fixed at 100 ms and +100 mV millivolts, respectively. The initial cycle was identified as the memorization phase, while the following cycle were classified as relearning phases. After each cycle, a spontaneous relaxation decay, denoted as "τ", transpired, a phase typically known as the forgetting stage.[22,44]

Conflict of Interest

The authors declare no conflict of interest.

Author Contributions

D.S.A, V.K., and K.U.K.: Conceptualization, methodology, visualization, formal analysis, writing—original draft; H.H., V.C.S.T., and N.S.A.: software, resources, data curation; V.A.L.R, H.A.: conceptualization, supervision, funding acquisition, project administration, writing—review and editing.

Data Availability Statement

The data that support the findings of this study are available from the corresponding author upon reasonable request.

[1] W. Shi, Y. Guo, Y. Liu, *Adv. Mater.* **2020**, *32*, 1901493.

[2] F. Torres, A. C. Basaran, I. K. Schuller, *Adv. Mater.* **2023**, https://doi.org/10.1002/adma.202205098.

[3] C. López, *Adv. Mater.* **2022**, *35*, 2208683.

[4] K. Sun, J. Chen, X. Yan, *Adv. Funct. Mater.* **2021**, *31*, 2006773.

[5] X. Liu, F. Wang, J. Su, Y. Zhou, S. Ramakrishna, *Adv. Funct. Mater.* **2022**, *32*, 2113050.

[6] J. Q. Yang, R. Wang, Y. Ren, J. Y. Mao, Z. P. Wang, Y. Zhou, S. T. Han, *Adv. Mater.* **2020**, *32*, 2003610.

[7] Y. Sun, Y. Ding, D. Xie, *Adv. Funct. Mater.* **2021**, *31*, 2105625.

[8] Y. Guo, F. Wu, G. H. Dun, T. Cui, Y. Liu, X. Tan, Y. Qiao, M. Lanza, H. Tian, Y. Yang, T. L. Ren, *Adv. Funct. Mater.* **2023**, *33*, 2208055.

[9] Y. Lee, J. Y. Oh, T. W. Lee, *Adv. Mater. Technol.* **2022**, *7*, 2200193.

[10] Q. Wan, M. T. Sharbati, J. R. Erickson, Y. Du, F. Xiong, *Adv. Mater. Technol.* **2019**, *4*, 1900037.

[11] K. Byun, I. Choi, S. Kwon, Y. Kim, D. Kang, Y. W. Cho, S. K. Yoon, S. Kim, *Adv. Mater. Technol.* **2022**, https://doi.org/10.1002/admt.202200884.

[12] M. J. Gilbert, *Commun. Phys.* **2021**, *4*, 70.

[13] C. Wang, G. Q. Mao, M. Huang, E. Huang, Z. Zhang, J. Yuan, W. Cheng, K. H. Xue, X. Wang, X. Miao, *Adv. Sci.* **2022**, *9*, 2201446.

[14] H. Liu, Y. Qin, H. Chen, J. Wu, J. Ma, Z. Du, N. Wang, J. Zou, S. Lin, X. Zhang, Y. Zhang, H. Wang, *Adv. Mater.* **2023**, https://doi.org/10.1002/adma.202205047.

[15] I. Tzouvadaki, P. Gkoupidenis, S. Vassanelli, S. Wang, T. Prodromakis, *Adv. Mater.* **2023**, https://doi.org/10.1002/adma.202210035.

[16] X. Pan, T. Jin, J. Gao, C. Han, Y. Shi, W. Chen, *Small* **2020**, *16*, 2001504.

[17] D. Mishra, K. Mokurala, A. Kumar, S. G. Seo, H. Bin Jo, S. H. Jin, *Adv. Funct. Mater.* **2023**, *33*, 2211022.

[18] B. Li, W. Wei, L. Luo, M. Gao, Z. G. Yu, S. Li, K. W. Ang, C. Zhu, *Adv. Electron. Mater.* **2022**, *8*, 2200089.

[19] V. Karthikeyan, V. C. S. Theja, M. M. De Souza, V. A. L. Roy, *Phys. Status Solidi RRL* **2022**, *16*, 2100419.

[20] X. Chen, B. Chen, B. Jiang, T. Gao, G. Shang, S. T. Han, C. C. Kuo, V. A. L. Roy, Y. Zhou, *Adv. Funct. Mater.* **2023**, *33*, 2208807.

[21] S. R. Zhang, L. Zhou, J. Y. Mao, Y. Ren, J. Q. Yang, G. H. Yang, X. Zhu, S. T. Han, V. A. L. Roy, Y. Zhou, *Adv. Mater. Technol.* **2019**, *4*, 1800342.

[22] D. S. Assi, H. Huang, V. Karthikeyan, V. C. S. Theja, M. M. de Souza, N. Xi, W. J. Li, V. A. L. Roy, *Adv. Sci.* **2023**, https://doi.org/10.1002/advs.202300791.

[23] M. Y. Tsai, K. C. Lee, C. Y. Lin, Y. M. Chang, K. Watanabe, T. Taniguchi, C. H. Ho, C. H. Lien, P. W. Chiu, Y. F. Lin, *Adv. Funct. Mater.* **2021**, *31*, 2105345.

[24] X. B. Yan, J. H. Zhao, S. Liu, Z. Y. Zhou, Q. Liu, J. S. Chen, X. Y. Liu, *Adv. Funct. Mater.* **2018**, *28*, 1705320.

[25] L. Yuan, S. Liu, W. Chen, F. Fan, G. Liu, *Adv. Electron. Mater.* **2021**, *7*, 2100432.

[26] G. Lee, J. H. Baek, F. Ren, S. J. Pearton, G. H. Lee, J. Kim, *Small* **2021**, *17*, 2100640.

[27] N. Raeis-Hosseini, Y. Park, J.-S. Lee, *Adv. Funct. Mater.* **2018**, *28*, 1800553.

[28] S. Ling, C. Zhang, C. Ma, Y. Li, Q. Zhang, *Adv. Funct. Mater.* **2023**, *33*, 2208320.

[29] N. Ilyas, J. Wang, C. Li, D. Li, H. Fu, D. Gu, X. Jiang, F. Liu, Y. Jiang, W. Li, *Adv. Funct. Mater.* **2022**, *32*, 2110976.

[30] C. Han, X. Han, J. Han, M. He, S. Peng, C. Zhang, X. Liu, J. Gou, J. Wang, *Adv. Funct. Mater.* **2022**, *32*, 2113053.

[31] Y. Hu, M. Dai, W. Feng, X. Zhang, F. Gao, S. Zhang, B. Tan, J. Zhang, Y. Shuai, Y. Q. Fu, P. A. Hu, *Adv. Mater.* **2021**, *33*, 2104960.

[32] H. Lee, M. Jin, H. J. Na, C. Im, J. H. Lee, J. Kim, Y. J. Gong, C. Lee, E. Lee, Y. S. Kim, *Adv. Funct. Mater.* **2022**, *32*, 2110591.

[33] X. Wang, Y. Zong, D. Liu, J. Yang, Z. Wei, *Adv. Funct. Mater.* **2023**, *33*, 2213894.

[34] R. M. Shiffrin, R. C. Atkinson, *Psychol. Rev.* **1969**, *76*, 179.

[35] L. Yin, R. Cheng, Y. Wen, C. Liu, J. He, *Adv. Mater.* **2021**, *33*, 2007081.

[36] D. Hao, Z. Yang, J. Huang, F. Shan, *Adv. Funct. Mater.* **2023**, *38*, 2211467.

[37] C. Ban, Z. Zhang, C. Song, H. Zhang, X. Luo, X. Wang, J. Liu, Z. Liu, W. Huang, *Adv. Mater. Technol.* **2023**, *8*, 2200870.

[38] Y. Wang, L. Yin, W. Huang, Y. Li, S. Huang, Y. Zhu, D. Yang, X. Pi, *Adv. Intell. Syst.* **2021**, *3*, 2000099.

[39] W. C. Yang, Y. C. Lin, S. Inagaki, H. Shimizu, E. Ercan, L. C. Hsu, C. C. Chueh, T. Higashihara, W. C. Chen, *Adv. Sci.* **2022**, *9*, 2105190.

[40] Y. Li, J. Wang, Q. Yang, G. Shen, *Adv. Sci.* **2022**, *9*, 2202123.

[41] P. Lei, H. Duan, L. Qin, X. Wei, R. Tao, Z. Wang, F. Guo, M. Song, W. Jie, J. Hao, *Adv. Funct. Mater.* **2022**, *32*, 2201276.

[42] D. Hao, D. Liu, J. Zhang, Y. Wang, J. Huang, *Adv. Mater. Technol.* **2021**, *6*, 2100678.

[43] H. L. Park, Y. Lee, N. Kim, D. G. Seo, G. T. Go, T. W. Lee, *Adv. Mater.* **2020**, *32*, 1903558.

[44] D. S. Assi, M. P. Haris, V. Karthikeyan, S. Kazim, S. Ahmad, V. A. L. Roy, *Adv. Electron. Mater.* **2023**, https://doi.org/10.1002/aelm.202300285.

[45] H. Li, X. Jiang, W. Ye, H. Zhang, L. Zhou, F. Zhang, D. She, Y. Zhou, S. T. Han, *Nano Energy* **2019**, *65*, 104000.

[46] S. J. Kim, T. H. Lee, J. M. Yang, J. W. Yang, Y. J. Lee, M. J. Choi, S. A. Lee, J. M. Suh, K. J. Kwak, J. H. Baek, I. H. Im, D. E. Lee, J. Y. Kim, J. Kim, J. S. Han, S. Y. Kim, D. Lee, N. G. Park, H. W. Jang, *Mater. Today* **2022**, *52*, 19.

[47] H. K. He, R. Yang, W. Zhou, H. M. Huang, J. Xiong, L. Gan, T. Y. Zhai, X. Guo, *Small* **2018**, *14*, 1800079.

[48] H. L. Park, H. Kim, D. Lim, H. Zhou, Y. H. Kim, Y. Lee, S. Park, T. W. Lee, *Adv. Mater.* **2020**, *32*, 1906899.

[49] H. Ye, Z. Liu, H. Han, T. Shi, G. Liao, *Mater. Adv.* **2022**, *3*, 7248.

[50] C. M. Yang, T. C. Chen, D. Verma, L. J. Li, B. Liu, W. H. Chang, C. S. Lai, *Adv. Funct. Mater.* **2020**, *30*, 2001598.

[51] S. Dai, X. Wu, D. Liu, Y. Chu, K. Wang, B. Yang, J. Huang, *ACS Appl. Mater. Interfaces* **2018**, *10*, 21472.

[52] W. Xu, H. Cho, Y. H. Kim, Y. T. Kim, C. Wolf, C. G. Park, T. W. Lee, *Adv. Mater.* **2016**, *28*, 5916.

[53] R. Yu, E. Li, X. Wu, Y. Yan, W. He, L. He, J. Chen, H. Chen, T. Guo, *ACS Appl. Mater. Interfaces* **2020**, *12*, 15446.

[54] H. Xiong, L. Xu, C. Gao, Q. Zhang, M. Deng, Q. Wang, J. Zhang, D. Fuchs, W. Li, A. Cui, L. Shang, K. Jiang, Z. Hu, J. Chu, *ACS Appl. Mater. Interfaces* **2021**, *13*, 50132.